Nanoscale

PAPER

View Article Online
View Journal | View Issue

Cite this: *Nanoscale*, 2023, **15**, 17534

pH-Responsive swimming behavior of light-powered rod-shaped micromotors†

Srikanta Debata,[a] Suvendu Kumar Panda,[a] Satyaprakash Trivedi,[a] William Uspal*[b] and Dhruv Pratap Singh *[a]

Received 31st July 2023,
Accepted 2nd October 2023

DOI: 10.1039/d3nr03775d

rsc.li/nanoscale

Micromotors have emerged as promising devices for a wide range of applications *e.g.*, microfluidics, lab-on-a-chip devices, active matter, environmental monitoring, *etc*. The control over the activity of micromotors with the ability to exhibit multimode swimming is one of the most desirable features for many of the applications. Here, we demonstrate a rod-shaped light-driven micromotor whose activity and swimming behavior can easily be controlled. The rod-shaped micromotors are fabricated through the dynamic shadowing growth (DSG) technique, where a 2 μm long arm of titanium dioxide (TiO_2) is grown over spherical silica (SiO_2) particles (1 μm diameter). Under low-intensity UV light exposure, the micromotors exhibit self-propulsion in an aqueous peroxide medium. When activated, the swimming behavior of micromotors greatly depends on the pH of the medium. The swimming direction, *i.e.*, forward or backward movement, as well as swimming modes like translational or rotational motion, can be controlled by changing the pH values. The observed dynamics has been rationalized using a theoretical model incorporating chemical activity, hydrodynamic flow, and the effect of gravity for a rod-shaped active particle near a planar wall. The pH-dependent translational and rotational dynamics of micromotors provide a versatile platform for achieving controlled and responsive behaviors. Continued research and development in this area hold great promise for advancing micromotors and enabling novel applications in microfluidics, micromachining, environmental sciences, and biomedicine.

1. Introduction

Micromotors are micrometer-size artificial agents that can swim through a fluid medium. Considering their potential applications in various important areas, *e.g.*, targeted drug delivery,[1] cargo transportation in microfluidic channels,[2] environmental monitoring,[3] dynamic self-assembly,[4] active matter,[5–7] *etc.*, the design and fabrication of micromotors have received significant interest from researchers in recent years. One of the key prerequisites of the design of functional micromotors is stimuli–responsive behavior. Several micromotor designs that respond to external stimuli such as light,[8] electric fields,[9] magnetic fields,[10] and sound[11] have been reported. When stimulated, these micromotors show interesting dynamics, ranging across tactic responses,[12,13] self-organization,[14,15] guided swimming,[16] manipulation or transportation of microparticles,[17] *etc*. All these features are interesting for several promising applications. However, it is to be noted that these stimulations need an external source and control, which limits their autonomy. Here, one possibility is to think about designs that are responsive to the surrounding medium, which is a behavior typically seen in microorganisms as they modify their activity, swimming dynamics, or organizational behavior in response to changes in the properties, *e.g.*, pH value or ion concentration, of the fluid medium.[18–20]

Recently, some experimental studies have demonstrated pH-responsive micromotor designs, *e.g.*, Singh *et al.* showed that light-driven micromotors form dynamic clusters at high pH values.[21] Möller *et al.* reported self-assembly-driven multiparticle micromotors that swim in pH gradients and help in mapping the pH field in the medium.[22,23] By working on biohybrid systems and incorporating *E. coli* bacteria, Zhuang *et al.* formed pH-tactic micromotors.[24] Similarly, in another study, Heckel *et al.* demonstrated star-shaped light-driven microparticles that exhibit pH-dependent swimming behavior.[25] These studies exhibit pH-responsive behavior; however, they involve complex micromotor structures, limited dynamics, or tedious experimental procedures, which limit their applications.

---

[a] *Department of Physics, IIT Bhilai, Kutelabhata, Durg, Chhattisgarh, 491001, India. E-mail: dhruv@iitbhilai.ac.in*
[b] *Department of Mechanical Engineering, University of Hawai'i at Mānoa, 2540 Dole Street, Holmes Hall 302, Honolulu, HI 96822, USA. E-mail: uspal@hawaii.edu*

† Electronic supplementary information (ESI) available: Videos S1–S3 and Fig. S1–S5. See DOI: **https://doi.org/10.1039/d3nr03775d**

The role of pH in governing the dynamics has also not been thoroughly discussed.

In this study, we present light-driven rod-shaped micromotors that show bimodal motility and swimming direction reversibility, depending on the pH value of the medium. The rod-shaped micromotors are fabricated by taking advantage of Dynamic Shadowing Growth (DSG) in an e-beam evaporation chamber equipped with a glancing angle deposition (GLAD)[15,26–29] system. The design consists of a microrod-like shape having silica (SiO_2) and titania (TiO_2) materials as passive (head) and active (tail) components, respectively. When illuminated with a low intensity (76 mW cm^{-2}) UV light (320–400 nm), the micromotors show motility in an aqueous peroxide medium. However, the swimming behavior greatly depends on the pH of the medium. At low (acidic) pH values, the micromotors swim towards the passive head and exhibit linear or translational motion. However, at higher pH (basic) values, they reverse the swimming direction to move towards the active tail and interestingly switch to rotational motion. The observed pH-dependent dynamics are rationalized using a theoretical model incorporating chemical activity, hydrodynamic flow, and the effect of gravity for a rod-shaped active particle near a planar wall. The study presents a simple experimental design that is supported by theoretical modeling for the light-controlled and pH-responsive micromotors. We believe that these micromotors could be interesting for applications like pH sensing or mapping in microfluidic systems, on-demand local mixing of fluids, targeted drug delivery, *etc.*

2. Materials and methods

2.1 Fabrication of rod-shaped micromotors

The rod-shaped micromotors are fabricated by taking advantage of dynamic shadowing growth (DSG).[28–34] The schematic in Fig. 1 shows the steps involved in the fabrication. Briefly, first, a close-packed monolayer of silica particles (1 μm diameter, Micromod) was formed upon the silicon substrate using the Langmuir–Blodgett (LB) technique. For the LB technique, the silica particles were made hydrophobic by treating their surface with the allyltrimethoxysilane (Sigma Aldrich) chemical. The chemically treated microparticles were dispersed over the water surface in an LB trough to form a monolayer at the interface. The formed monolayer was transferred over the silicon (Si) substrates by slowly pulling the substrates out of the LB trough as shown in Fig. 1a. The monolayer over the silicon substrate (see Fig. 1b) acts like a seed layer for the dynamic shadowing growth. For the growth, the patterned substrate was then transferred into a high-vacuum chamber (~10^{-6} Torr) consisting of a glancing angle deposition (GLAD) assisted e-beam evaporation system. The substrates were mounted on a specially designed sample holder that holds the substrates making a very high angle (86°) between the substrate normal and the direction of the incident vapor flux, and rotates (10 RPM) them in the azimuthal plane.[35–37] We evaporated titanium dioxide (TiO_2) in the chamber at a deposition rate of 0.1 nm s^{-1}. The dynamic shadowing at the tilted and rotating substrates allows TiO_2 to form vertical rods over the individual seeds (see Fig. 1c and d). The as-grown TiO_2 is normally amorphous, and to convert it into the active anatase phase, the fabricated Janus micromotors were annealed at 450 °C for 30 min in air. The formation of the anatase phase was confirmed through powder X-ray diffraction (PXRD, Bruker D8) and UV-vis absorbance spectra (see Fig. S1, ESI†). The formation of the rod-like shape and elemental distribution over its surface were confirmed using field-emission scanning electron microscopy (Fe-SEM, Zeiss Gemini 500) imaging and energy dispersive X-ray spectroscopy (EDX) analysis, respectively.

2.2 Sample preparation

Once the microrods were formed, they were transferred to an aqueous medium by sonicating the substrates in water. When they were transferred, a small amount of hydrogen peroxide (H_2O_2) was added to make an aqueous solution of 5% (v/v) H_2O_2. For changing the pH of the solution to make it basic or acidic, a small amount of diluted tetramethyl ammonium hydroxide or sulfuric acid was added, respectively.

2.3 Illumination and observation

A sessile droplet of the microrods with 5% (v/v) aqueous hydrogen peroxide (H_2O_2) solution was deposited on a plasma-cleaned glass coverslip and the particles were allowed to sediment. The experiment was performed under a 63× objective lens arranged in the inverted geometry mode of an optical microscope (Leica DMi8). A mercury lamp (HBO 103) in an epi-fluorescence-type arrangement served as the light source for the photocatalytic excitation and a white LED in transmittance mode was used for the sample imaging. A set of optical filters was used to allow light of wavelengths 320 nm to 400 nm for the excitation and above 400 nm white light for the imaging of the micromotors, respectively. The intensity of excitation light was maintained at 76 mW cm^{-2} throughout the experiment. The images were captured at frame rates ranging from 10 to 20 fps. To calculate the Mean Squared Displacement (MSD), we recorded a video of each particle, capturing hundreds of frames within a field of view measuring approximately 125 μm × 125 μm. Particle tracking provides the position data of each particle in the captured frames. By using the data points, MSD was calculated mathematically and plotted at different time intervals.[38] A self-written Python code based on the CSRT tracker provided in the Open-Source Computer Vision Library was used for tracking and measuring the speed of micromotors, and the details are provided somewhere else.[17]

2.4 Theoretical model

Section 3 of the ESI† provides the detailed mathematical formulation of the model. Briefly, we adapted a continuum model common in the active colloid literature that resolves the shape of the particle, the distribution of catalytic activity on the particle surface, and the chemical and flow fields sourced

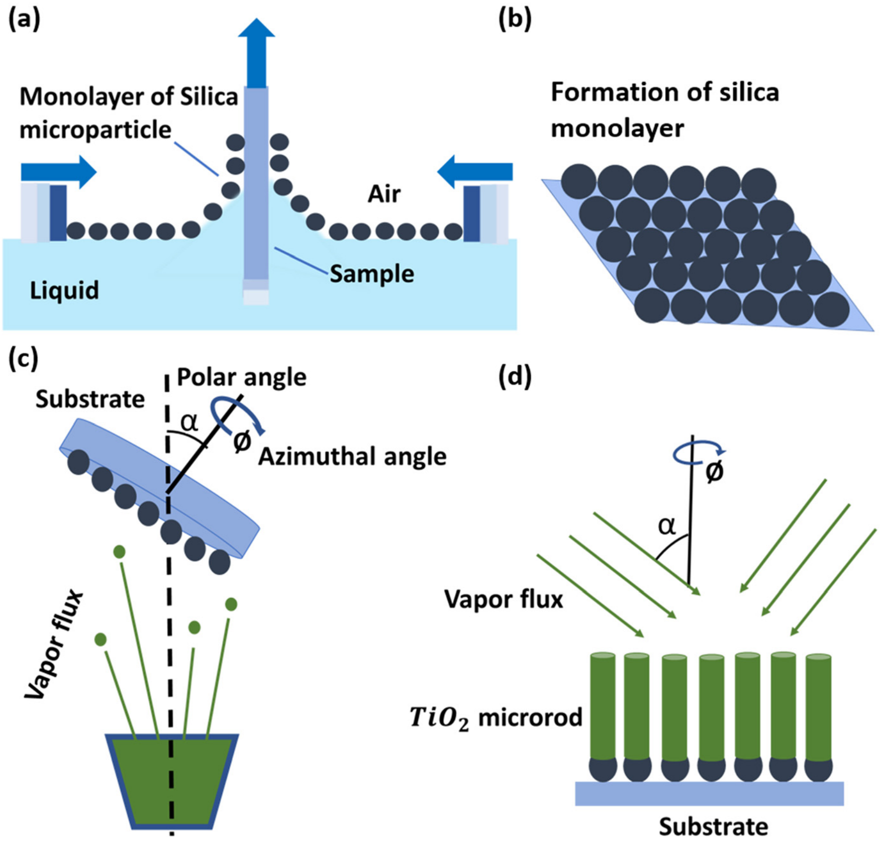

Fig. 1 Fabrication of rod-shaped micromotors. (a) Schematic representation of the Langmuir Blodgett (LB) technique for the monolayer formation of silica microparticles. (b) Schematic of the silica microparticle monolayer over the Si substrate. (c) Schematic representation of rod formation by glancing angle deposition (GLAD) using the DSG technique. (d) Dynamic shadowing at a very high vapor incidence angle (α) on a rotating substrate leads to the growth of vertical rods.

by the particle.[39,40]The particle is assumed to produce a chemical product ("solute") on TiO_2 at a uniform rate. Using the boundary element method, we numerically solve for the concentration of the solute $c(\vec{x})$. For a particle in the vicinity of a hard planar substrate (*i.e.*, "wall"), we include the effect of the wall on $c(\vec{x})$. The interfacial gradients of the solute concentration on the particle surface are assumed to drive an interfacial fluid flow $\vec{u}_s(\vec{x})$ ("slip velocity") *via* a phoretic mechanism.[41] We assume Stokes flow and solve for the flow field $\vec{u}_s(\vec{x})$ and particle velocities $\vec{U}$ and $\vec{\Omega}$ numerically, including the effect of the no-slip wall. We also include the effect of gravity and a short-ranged repulsive potential between the particle and the wall.[42]

3. Results and discussion

3.1 Light-powered rod-shaped micromotors

The rod-shaped micromotors are fabricated using dynamic shadowing growth (DSG). DSG occurs in the glancing angle deposition (GLAD) system, where the substrate is placed so that its normal has a very high angle ($\alpha \geq 85°$) with respect to the incident vapor flux direction.[26,27] The details of the fabrication process are given in the 'Materials and methods' section. The fabrication technique allows the fabrication of a large number of uniform, vertically standing, and close-packed microrods of length ~3 μm and diameter ~1 μm over the silicon (Si) substrate. The presence of a spherical seed particle and a grown rod-like component over it can be seen in the SEM image (see Fig. 2a).The EDX mapping (see Fig. 2b) confirms the growth of TiO_2 material over the silica seed particles, showing the material distribution. They can be considered as the head (silica) and tail (TiO_2) parts of the microrods. Previously, it has been observed that the crystalline phase of TiO_2 shows a better photo-response.[12,43] Here, the post-fabrication sample treatment converts the as-grown amorphous TiO_2 column into the crystalline anatase phase. The phase transformation is verified through the XRD analyses as shown in Fig. 2c. It is to be noted that the present fabrication technique allows the formation of a large number of micromotors in a single deposition. Typically, a 4-inch diameter Si substrate can be coated with micromotors at a number density of around 10^6 mm^{-2}. This number suggests that a sufficient quantity of micromotors can be fabricated in a single batch that might be required for any typical application.

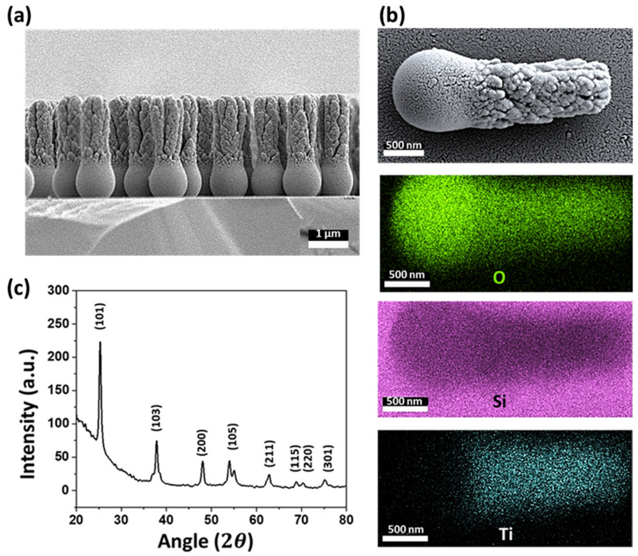

Fig. 2 Characterization of rod-shaped micromotors. (a) Cross-sectional SEM view of micromotors. (b) EDX mapping showing the elemental distribution over fabricated micromotors. (c) XRD analysis shows the phase transformation of TiO_2 after annealing.

Once the characterization is done, the rod-shaped micromotors were transferred into water through sonication for performing the experiments. The grown rod-shaped micromotors show Brownian fluctuations when immersed in an aqueous peroxide solution (5% v/v) under no light illumination. Upon turning on the UV light (320–400 nm, 76 mW cm^{-2} intensity), the photocatalytic decomposition of peroxide occurs on the TiO_2 surface according to the reaction scheme shown in eqn (1).

$$\begin{aligned} &\mathrm{TiO_2} + h\nu \rightarrow \mathrm{h^+} + \mathrm{e^-} \\ &\mathrm{H_2O_2} + 2\mathrm{h^+} \rightarrow \mathrm{O_2} + 2\mathrm{H^+} \\ &\mathrm{H_2O_2} + 2\mathrm{e^-} + 2\mathrm{H^+} \rightarrow 2\mathrm{H_2O} \end{aligned} \tag{1}$$

Consequently, the asymmetric chemical activity over the microrods drives the solution out of the chemical equilibrium, and the formed gradient in the surrounding chemical composition results in a self-phoretic motion of the microrods.[17,21] The observed swimming behavior of the fabricated rod-shaped micromotors is discussed in the following section. Since the chemical activity over TiO_2 is driven by light, the micromotors swim only when the light is turned on. Under no light, they remain idle and exhibit Brownian motion (see Fig. 3a). In addition to the light conditions, the swimming behavior of these light-driven rod-shaped micromotors is found to vary significantly upon changing the pH of the medium.

3.2 pH-Dependent dynamics of rod-shaped micromotors

The pH of the aqueous peroxide medium (5% v/v) is slightly acidic (~5.5). In this medium, when illuminated with UV light, the micromotors swim in random directions, making long trajectories at an average speed of 3.7 ± 0.75 μm s^{-1}. This motion can be considered translational for short ranges, because for longer times, the thermal fluctuations lead to deviations from the straight-line motion. The microscopic images show that the motion of micromotors is toward the silica head, *i.e.*, away from the active TiO_2 tail. On reducing the pH to 4, the overall swimming behavior remains the same; however, the average

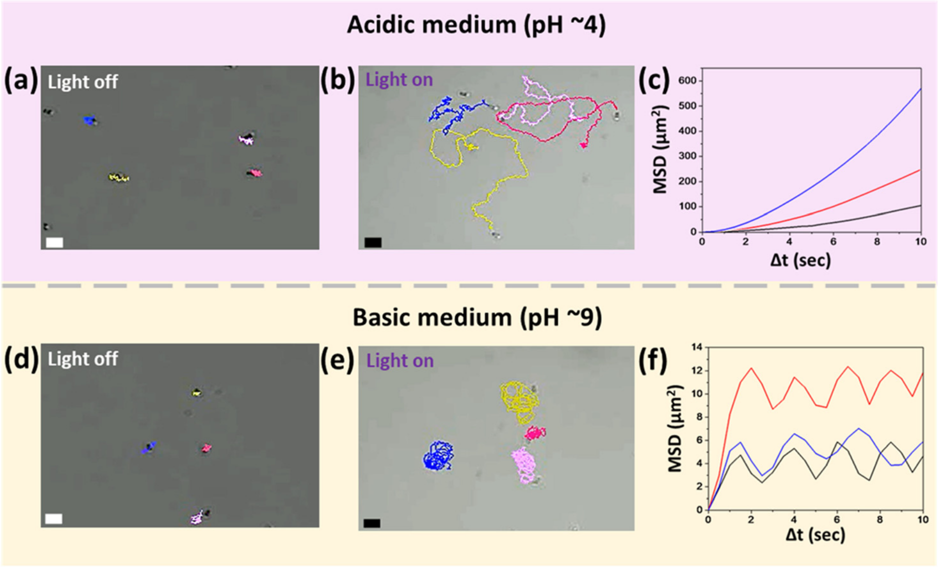

Fig. 3 pH-Dependent dynamics of micromotors. (a) Micromotors under the light-off conditions in an acidic medium. (b) Trajectories show the translational motion of the micromotors in an acidic medium when the light is turned on. (c) Mean square displacement *vs.* time interval graph for translation. Three different color plots correspond to three different micromotors (d) random Brownian fluctuations of micromotors under light-off conditions. (e) Micromotors exhibiting rotational dynamics as shown by the trajectories in a basic medium under light-on conditions. (f) MSD *vs.* time interval plot of the rotating micromotors. Scale bar represents 5 μm length.

translational speed increases to around 4.5 ± 1.2 μm s^{-1}, which is close to 1.5 times the body length per second (see Video S1, ESI†). The trajectories and mean square displacement (MSD) *versus* time interval plot of micromotors at pH 4 are shown in Fig. 3b and c, respectively. They confirm that the micromotor exhibits random trajectories with high directional persistence. In Fig. 3c, each MSD plot is for an individual micromotor produced by averaging the displacement of particles over the progression of time intervals. A detailed discussion on the nature of the MSD plot[38,44] and associated features like persistence length and time scale for transition to the diffusive regime is provided in the ESI† (see section 2.3, ESI†).

On increasing the pH, we initially observe a reduction in speed. Interestingly, above the neutral value, *i.e.*, pH 7, the direction of motion is reversed, and the micromotors swim toward the active TiO_2 tail, *i.e.*, away from the inert silica head. In addition to the change in the swimming direction, on increasing the pH, it was observed that when activated, instead of making long trajectories, the micromotors remain confined to the small region around their initial positions (see Video S2, ESI†). This effect becomes more pronounced and changes into rotational motion on further increasing the pH (see Video S3, ESI†). Fig. 3e shows that the micromotors perform the rotational motion at pH 9. The MSD *vs.* time interval plot with multiple peaks also indicates the cyclic or rotational motion of the micromotors (see Fig. 3f). It can be noticed that, while the micromotors are rotating, thermal fluctuations or asymmetry in the shape or the flows around the micromotors may cause slight variations in the rotational path, and that is why they slightly deviate from repeating the same path around a fixed point. This is evident from the trajectories and MSD plot given in Fig. 3e and f, respectively.

To compare the two cases, *i.e.*, pH 4 and pH 9, the images of a micromotor moving in media at these pH values for a given time interval are shown in Fig. 4a and b, respectively. The images clearly indicate that for the given time interval, at low pH, the micromotor exhibits translational motion, while at high pH, it rotates and completes a full rotation about its own body axis. The schematic in Fig. 4c shows a cartoon representing this overall swimming behavior of the micromotors, *i.e.*, no motion when light is turned off, translational motion under light illumination at low pH, and rotational motion under light illumination and high pH conditions (see section 2.4, ESI†). The observed direction of movement at different pH values is highlighted with the brown color arrows. At low pH, it is towards the head, while at high pH (9), it reverses toward the tail. The length of the arrows is kept different to highlight the dominating mode, *i.e.*, translation or rotational at different pH values.

To understand the mechanisms behind this phenomenology and in particular the dependencies on the pH of the medium, in the next section, we develop and study a theoretical model that phenomenologically accounts for the pH-dependent interactions of the chemical species (reactant/product) with the micromotor's surface. These interactions govern the strength and direction of flows around them.

3.3 Theoretical model

We aim to develop a simple phenomenological model that recovers the pH-dependent transition from fast "head-forward"

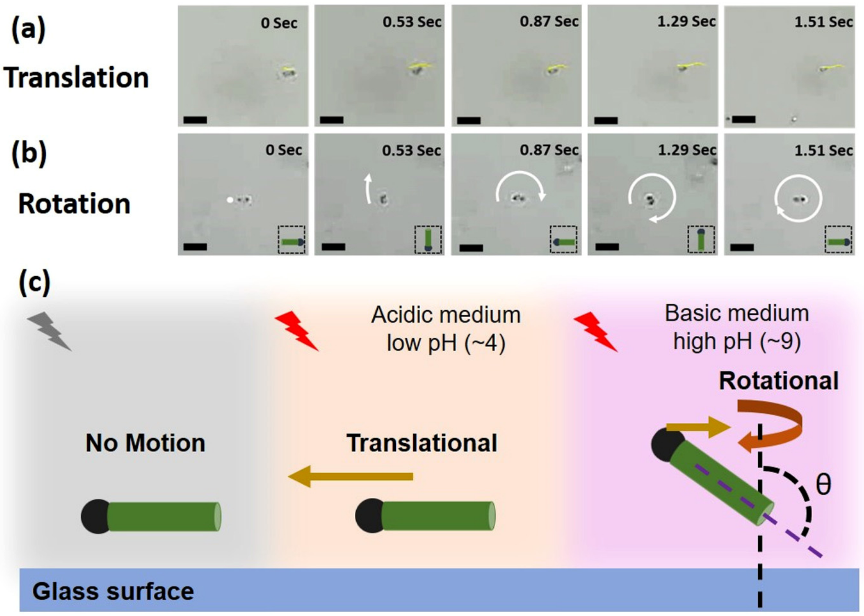

Fig. 4 Multimode dynamics of a rod-shaped micromotor. (a) The translational motion of a micromotor with the trajectory at different time frames. (b) The rotational motion of a micromotor with orientations at different time frames. (c) Schematic representation of micromotor motion under light off/on conditions and the nature of motion with respect to pH of the medium. The rotational motion of a micromotor at high pH with tilted orientation (tilt angle 'θ') of the body axes (dotted purple line) with respect to the surface normal (dotted black line) is highlighted. This is in accordance with the theoretical model developed.

motion, with the rod axis parallel to the substrate, to slow "tail-forward" motion, with a tilted angle of the rod axis. Our model resolves the complex shape of the particle, the difference in the material composition between the two particle segments, the chemical activity of the particle, particle-generated flows, and the effect of the confining wall. For simplicity, we assume that there is uniform, steady production of a product molecule (*i.e.*, oxygen) over the TiO_2 segment of the particle, *i.e.*, we neglect the details of the reaction scheme in eqn (1). As discussed in detail in the ESI†, spatial variations in the product molecule concentration along the surface of the particle lead to fluid flow in a thin interfacial region, modeled as an effective slip velocity on the particle surface. This slip velocity drives the flow in the surrounding solution, leading to particle motion. Importantly, the slip velocity at a location on the particle surface is proportional to a material-dependent parameter, the so-called surface mobility. This parameter provides the details of the effective interaction between the product molecule and the particle surface.[45] Here, we assume that the surface mobility takes constant values on the "head" and "tail" of the particle. Our model additionally includes the effect of gravity (force and torque) on the particle. We show that the pH-driven transition can be recovered in the model as an effective change in the surface mobilities, *i.e.*, the particle surface chemistry.

3.3.1 Particle in free space (unbound solution).

Fig. 5a shows the geometry of the particle, as well as the concentration of the reaction product $c(\vec{x})$ on the surface of the particle and in the surrounding fluid for a particle in unbound solution (*i.e.*, the particle is far away from binding surfaces). In our model, the surface chemistry of the particle is parameterized by two dimensionless quantities, b_i and b_c, corresponding to the inert "head" and the catalytic "tail", respectively. Specifically, they parameterize the interaction between the reaction product and the surface. When a surface mobility parameter is negative, the interaction is effectively repulsive; when it is positive, the interaction is effectively attractive. In terms of the characteristic velocity U_0 (see the ESI†), we calculated that the velocity of the particle in free space is $U_{fs}/U_0 = 0.0943b_i - 0.0298b_c$, where a positive velocity corresponds to "tail-forward" motion. Thus, negative (*i.e.*, repulsive) b_i would contribute to driving the particle in the negative z direction, away from the catalytic tail. Intuitively, for repulsive b_i, the spherical head is driven away from the high concentration of the solute in the region of the tail. Likewise, positive (*i.e.*, attractive) b_c would contribute to driving the particle in the negative z direction, away from the catalytic tail. This is less intuitive, but can be understood from the fact that the solute concentration is high along the sides of the rod and low at the tip. In Fig. 5a and b, we also show the streamlines of the flow for the specific values $b_c = 1$ and $b_i = 0.25$. (Note that the concentration field does not depend on the values of b_i and b_c.) These parameters correspond to "head-forward" motion, as indicated by the large white arrows. From the pattern of streamlines, it can be inferred that the particle is a hydrodynamic "pusher" for these parameters.[46] In particular, the particle draws fluid into the rod-like center region, and pushes fluid away from its two poles. The overall strength of the product/surface interaction is characterized with a characteristic surface mobility b_0, which has units of $m^5\ s^{-1}$ and contributes to the determination of $U_0 = |b_0\kappa/D|$, where κ is the rate of catalytic activity, and D is the diffusion coefficient of the product molecule (see the ESI†). In Fig. 5b, the background color in the fluid surrounding the particle shows the magnitude of the flow velocity for the value $U_0 = 160\ \mu m\ s^{-1}$. Note that the velocity magnitude is on the order of $\mu m\ s^{-1}$, consistent with experimental velocities. Interestingly, the flow is the strongest near the rod tip and the sphere/rod junction, indicating that these are the most important regions of the particle surface in driving particle motion. Additionally, in Fig. 5b, the colors on the surface of the particle show the catalytic region (green) and the inert region (blue).

3.3.2 Particles near a planar wall: head-forward motion.

Now, we consider a particle near a planar wall. From the foregoing discussion, we anticipate that a change between the

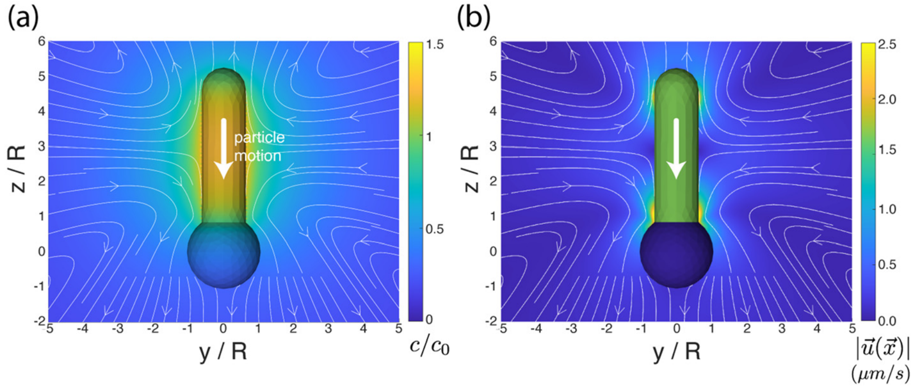

Fig. 5 Theoretical model of a micromotor in unbound solution. (a) Concentration field on the surface of the particle and in the bulk solution (color). The flow streamlines and white arrow showing the direction of motion correspond to the particular values of the surface mobility parameters, $b_c = 1$, $b_i = 0.25$. (b) The velocity magnitude for $b_c = 1$, $b_i = 0.25$, and $U_0 = 160\ \mu\ m\ s^{-1}$. Here, the colors on the surface of the particle indicate the catalytic region (green) and the inert region (blue). The speed of the particle is $|U_{fs}| = 1\ \mu m\ s^{-1}$.

"tail-forward" and "head-forward" characters of motion could arise from a change in the signs of the b_i and b_c parameters, and/or their relative magnitudes. Likewise, a change in these parameters can affect the pusher/puller character of the hydrodynamic flow. For instance, for streamlines shown in Fig. 5a, the negation of both b_i and b_c to $b_c = -1$ and $b_i = -0.25$ would simply reverse the directions of the arrowheads, changing the particle from a "pusher" to a "puller". However, it is not obvious how the tilt angle θ of the particle with respect to the wall normal might be affected. (As described in the ESI†, θ is defined as the angle between the sphere-to-rod-tip axis and the wall normal, such that, for $\theta = 0$, the particle axis is aligned with the wall normal, with the spherical "head" close to the wall.) For the particle motion near the wall, we also include the force and torque on the particle from gravity, as well as a short-ranged repulsive force, as described in the ESI†. In Fig. 6a, we show a phase portrait in the space defined by the particle height h (position of the sphere center above the wall) and the tilt angle θ for the parameters $b_c = 1$ and $b_i = 0.25$. In other words, the interaction of the product molecule and the surface is attractive on both sides of the particle, but more attractive on the catalytic tail than on the inert sphere. Additionally, U_0 is chosen as $U_0 = 160\ \mu\text{m s}^{-1}$. (Note that changing U_0 will non-trivially affect the dynamics, because the dynamics emerges from an interplay of self-propulsion and gravity, as well as the repulsive force. Also note that the actual particle velocity is considerably less than U_0, as the equation for U_{fs}/U_0 given above shows.) The phase portrait shows the dynamical evolution of an initial particle configuration (h, θ). In the phase portrait, there is a dynamical attractor state in which the particle axis is nearly parallel to the wall ($\theta = 97.2°$), and the particle is very close to the wall ($h/R = 1.37$). In this state, the particle maintains a steady angle and height, and translates along the wall. For the choice of U_0, the particle velocity is $|U_y| = 7\ \mu\text{m s}^{-1}$. Moreover, the direction of the wall-parallel component of the motion is "head-forward", as shown by the background color. In Fig. 6b, we show the particle configuration and concentration field in this steady state.

3.3.3 Particles near a planar wall: transition to tail-forward motion. Now, we seek to recover the pH-induced transition from a fast-moving, wall-parallel, and head-forward state to a slow-moving, tilted, and tail-forward state. Notably, to produce the "tilt", the effects of self-propulsion will have to work against the effects of gravity, which favor a wall-parallel configuration with a small height. In Fig. 6c, we show the phase portrait for $b_c = -1$ and $b_i = -0.25$. Note that we have only changed the signs of these quantities from the previous case. We have also chosen a U_0 value that is five times smaller than U_0 in the previous case: $U_0 = 32\ \mu\text{m s}^{-1}$, corresponding to either less catalytic activity, a lower interaction strength b_0, or both. Counterintuitively, despite the weakened self-propulsion, the attractor in this portrait is located at a large height $h/R = 3.58$ and a large tilt angle $\theta = 113.4°$. On the other hand, the particle velocity in the steady state intuitively reduces to $|U_y| = 0.6\ \mu\text{m s}^{-1}$. As indicated by the background color, the character of motion in the attractor state is "tail-forward", in agreement with the experimental observations. Fig. 6d shows the particle configuration and concentration field in this steady state.

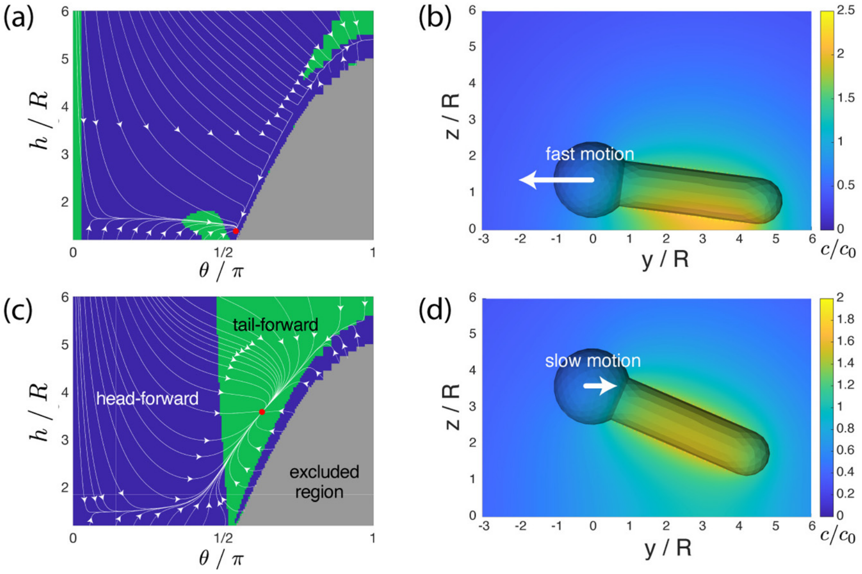

Fig. 6 Theoretical model of a micromotor near a wall. (a) Phase portrait with the height h/R and angle θ for a particle with $b_c = 1$, $b_i = 0.25$, and $U_0 = 160\ \mu\text{m s}^{-1}$. The angle θ is defined as the angle between the head-to-tail vector and the wall normal. There is a dynamical attractor (red dot) for a configuration in which the particle axis is nearly parallel to the wall ($\theta \approx 90°$) and is very close to the wall. The attractor is in the region (blue color) in which the direction of motion of the particle is towards the inert "head". In this configuration, the particle maintains a steady height and orientation. (b) Concentration field and particle configuration in the attractor configuration. The wall is located at $z = 0$. The particle "slides" along the wall with a steady speed $|U_y| = 7\ \mu\text{m s}^{-1}$. (c) Phase portrait for a particle with $b_c = -1$, $b_i = -0.25$, and $U_0 = 32\ \mu\text{m s}^{-1}$. There is a dynamic attractor in the region (green color) in which the particle motion is towards the catalytic "tail". In the attractor configuration, the particle axis is tilted with respect to the wall normal. (d) Concentration field and particle configuration in the attractor configuration. The particle has a slow "sliding" speed $|U_y| = 0.6\ \mu\text{m s}^{-1}$.

We have shown that the transition can be reproduced in a simple phenomenological model with a simple change in parameters. Firstly, the product/particle interaction is changed from effectively attractive to effectively repulsive – but the relative magnitudes of the oxygen/silica and oxygen/titania interactions are left unchanged. In our model, this corresponds to a simple sign inversion of two parameters. Secondly, the characteristic swimming speed $U_0 = |b_0\kappa/D|$ is reduced by a factor of five. Since a change in pH has little effect on the diffusion coefficient D of oxygen, this change in U_0 corresponds to a reduction of catalytic activity, a reduction of the magnitude of the surface/product interaction, or both. We suggest that both the sign inversion and the change in U_0 are consistent with a pH-induced change in the zeta potential on the surface of the particle. In this interpretation, the sign inversion corresponds to a change in the sign of the zeta potential, and a reduction of b_0 (thereby reducing U_0) corresponds to a change in the magnitude of the zeta potential.

The transition from a wall-parallel configuration to a tilted configuration with the sign inversion of the b_i and b_c parameters is consistent with the previously noted change from a hydrodynamic "pusher" to a hydrodynamic "puller". It is known from the literature that a pusher will tend to align its axis of propulsion to be within the plane of a no-slip wall through hydrodynamic interactions with the wall. Likewise, a puller will tend to align its axis to be perpendicular to the wall.[47]

Our modeling also demonstrates that, to reproduce the two surface-bound "sliding" states, it is sufficient to consider only a few essential physical parameters: the particle's weight and bottom-heaviness, and the activity-induced hydrodynamic and chemical interaction of the particle with the wall. Our results do not exclude the possibility that another choice of parameters, or a more detailed model, may reproduce the same transition, or even show better quantitative agreement with the experimental data. For instance, for a more finely tuned set of "high pH" parameters ($b_\mathrm{c} = -0.5$, $b_\mathrm{i} = -0.2$, $U_0 = 190\ \mu\mathrm{m\ s^{-1}}$), we obtain an attractor with an even stronger tilt angle, $\theta = 139°$, and a slow velocity of $|U_y| = 0.53\ \mu\mathrm{m\ s^{-1}}$, as shown in Fig. S2 (ESI†).† As an example of more detailed physics omitted from our model, we did not consider the chemiosmotic slip at the wall. Consideration of this effect could improve quantitative agreement with the experimental data but would introduce another free parameter (the surface mobility of the wall). Overall, our aim was to reproduce the steady states and the transition between them in the framework of a minimally featured model. The minimalism of our model suggests that pH-induced transitions between sliding states may be a generic phenomenon in active colloidal systems.

3.3.4 Particles near a planar wall: rotation. We briefly address the rotation observed in the experiments for the tilted state. Our model assumes an axisymmetric particle geometry and surface coating, and therefore cannot reproduce a non-zero component of angular velocity in the wall-normal direction. In experiments, the particle rotation is most likely due to imperfections in the particle geometry and coating. However, our model can help rationalize the transition between wall-parallel translation and circular motion. Consider an active particle moving in the xy plane with a fixed translational velocity U along a particle-defined axis, and fixed angular velocity Ω in the z direction. In the absence of thermal noise (Brownian motion), this particle will move in a circular orbit with the radius of curvature $R_\mathrm{c} = U/\Omega$. In the presence of thermal noise, and for large values of R_c (as compared with the persistence length of the particle direction), the tendency of the particle to move in circles will be overwhelmed by randomization of the particle direction by rotational Brownian motion. However, circular motion will be apparent for sufficiently small values of R_c. Thus, a pH-induced transition between the translation and circular motion can be understood as a pH-induced change in $R_\mathrm{c} = U/\Omega$. Now consider a transition between wall-parallel and tilted steady states. In such a transition, R_c will tend to decrease. Specifically, the tilting of the particle will significantly reduce the wall-parallel component of velocity U, as compared with U in the wall-aligned configuration of the particle. As an additional complication, the pH-dependence of the rotational Peclet number $\mathrm{Pe} = U_0/RD_\mathrm{r}$, characterizing the relative strength of swimming activity and rotational Brownian motion, will also have a role in this transition, by affecting the orientational persistence length. (Here, D_r is the rotational diffusion coefficient of the particle.) Thus, the "finely tuned" parameters discussed above ($b_\mathrm{c} = -0.5$, $b_\mathrm{i} = -0.2$, $U_0 = 190\ \mu\mathrm{m\ s^{-1}}$) may actually better reproduce the translation-to-rotation transition than the parameters in Fig. 6, because the fine-tuned parameters produce both a strong tilt angle and high value of U_0. Future modeling could probe the pH-induced change in R_c by breaking axisymmetry in the model, *e.g.*, by adding a geometric imperfection ("bump") to the particle or by introducing some non-axisymmetric spatial variations in catalytic activity on the particle tail.

3.3.5 Application to other experimental systems. In an interesting study conducted by Nicholls *et al.*, it was shown that the swimming behavior of similar rod-shape micromotors can be modulated by tuning the geometry of the micromotors.[48] They varied the aspect ratios of SiO_2/TiO_2 micromotors and found a maximum speed of $6 \pm 2\ \mu\mathrm{m\ s^{-1}}$ as well as reversibility in the swimming direction. However, in our study a single geometrical SiO_2/TiO_2 based rod shaped-micromotor is fabricated where a maximum speed of $4.5 \pm 1.2\ \mu\mathrm{m\ s^{-1}}$ is achieved under low intensity UV light illumination. Along with the active swimming, direction reversibility and transition from the translational to rotational motion of micromotors are achieved just by changing the pH of the medium and without altering the geometry. The experimental observation is further substantiated with a detailed theoretical study.

We briefly comment on the implications of our model for the interpretation of the data in Nicholls *et al.*'s study. Nicholls *et al.* hypothesize that a reversal in the direction of motion with changing tail length is due to the role of chemiosmotic flow on the wall. In the present study, for simplicity, we neglected the consideration of this chemiosmotic flow. Nevertheless, in the framework of our model, we find that it is possible to obtain a reversal of direction with a change of tail length for a particle in unbound solution (ESI Fig. S5†). On the other hand, for the tail lengths considered, this reversal effect occurs only within a relatively narrow band of surface mobility parameters. Overall, these findings point to the need for further studies that combine experiments and theoretical modeling in order to unravel the dependence of motion reversal and other phenomena on the various physical mechanisms that contribute to particle propulsion.

4. Conclusion

We have designed simple rod-shaped micromotors that can be fabricated inexpensively and very easily by using the dynamic shadowing growth (DSG) technique, and also large quantities can be obtained simultaneously. The structure comprises a TiO_2 microrod (2 μm) over a SiO_2 microsphere (1 μm diameter) which is activated through low intensity (76 mW cm^{-2}) UV light (320–400 nm) illumination in an aqueous peroxide medium. Interestingly, the micromotors exhibit multimode swimming behavior based on the pH of the medium. At lower pH (acidic ∼ 4), they show translatory motion with the swimming direction towards the silica head. On increasing the pH to around 9 (basic), they switch to rotational motion with the swimming direction reversed to the tail (TiO_2) side. The trajectories of motion and the mean square displacement (MSD) plots confirm the observed multimode swimming behavior of the micromotors in different pH media under UV light exposure. The pH-dependent multimode swimming has been rationalized using a theoretical model incorporating chemical activity, hydrodynamic flow, and the effect of gravity for a rod-shaped active particle near a planar wall. Experimental studies combined with theoretical modeling provides valuable insights into the role of the micromotor's structure, its surface properties, chemical activity, and the surrounding pH environment. This knowledge can be leveraged to optimize the design and performance of micromotors, tailoring them for specific applications in the field of environmental monitoring, lab-on-a chip devices, and microfluidics, and improving their overall efficiency.

Author contributions

D. P. S. conceptualized the problem statement; S. D. performed the experiments; S. D., S. K. P., and S. T. analyzed the data; W. U. conceptualized and performed the theoretical modeling; S. D., S. K. P., W. U., and D. P. S. wrote the manuscript. Credits: Srikanta Debata: investigation (lead), methodology (equal), validation (lead), writing – original draft (lead), and writing – review & editing (lead); Suvendu Kumar Panda: formal analysis (supporting), investigation (supporting), and writing – original draft (supporting); Satyaprakash Trivedi: formal analysis (supporting) and investigation (supporting); William Uspal: theoretical investigation (lead), conceptualization (supporting), writing – original draft (supporting), and writing – review & editing (supporting); Dhruv Pratap Singh: conceptualization (lead), investigation (supporting), methodology (supporting), project administration (lead), resources (lead), supervision (lead), writing – original draft (supporting), and writing – review & editing (supporting).

Conflicts of interest

The authors declare that they have no conflicts of interest.

Acknowledgements

Funding support by the SERB through the startup research grant (SRG/2020/001885) is greatly acknowledged. The authors SD and SP are grateful to MHRD, India for its financial support. We gratefully acknowledge technical support and advanced computing resources from University of Hawaii Information Technology Services – Cyberinfrastructure, funded in part by the National Science Foundation, Campus Cyberinfrastructure awards #2201428 and #2232862.

References

1 W. Gao and J. Wang, *Nanoscale*, 2014, **6**, 10486–10494.

2 J. Palacci, S. Sacanna, A. Vatchinsky, P. M. Chaikin and D. J. Pine, *J. Am. Chem. Soc.*, 2013, **135**, 15978–15981.

3 S. K. Panda, N. A. Kherani, S. Debata and D. P. Singh, *Mater. Adv.*, 2023, **4**, 1460–1480.

4 X. Peng, M. Urso, M. Ussia and M. Pumera, *ACS Nano*, 2022, **16**, 7615–7625.

5 A. Ziepke, I. Maryshev, I. S. Aranson and E. Frey, *Nat. Commun.*, 2022, **13**, 6727.

6 K. K. Dey and A. Sen, *J. Am. Chem. Soc.*, 2017, **139**, 7666–7676.

7 A. Zöttl and H. Stark, *J. Phys.: Condens. Matter*, 2016, **28**, 253001.

8 S. Palagi, D. P. Singh and P. Fischer, *Adv. Opt. Mater.*, 2019, **7**, 1900370.

9 J. G. Lee, A. Al Harraq, K. J. M. Bishop and B. Bharti, *J. Phys. Chem. B*, 2021, **125**, 4232–4240.

10 S. Yu, N. Ma, H. Yu, H. Sun, X. Chang, Z. Wu, J. Deng, S. Zhao, W. Wang, G. Zhang, W. Zhang, Q. Zhao and T. Li, *Nanomaterials*, 2019, **9**, 1672.

11 C. Dillinger, N. Nama and D. Ahmed, *Nat. Commun.*, 2021, **12**, 6455.

12 D. P. Singh, W. E. Uspal, M. N. Popescu, L. G. Wilson and P. Fischer, *Adv. Funct. Mater.*, 2018, **28**, 1706660.

13 B. Dai, J. Wang, Z. Xiong, X. Zhan, W. Dai, C.-C. Li, S.-P. Feng and J. Tang, *Nat. Nanotechnol.*, 2016, **11**, 1087–1092.

14 B. Yigit, Y. Alapan and M. Sitti, *Soft Matter*, 2020, **16**, 1996–2004.

15 S. Palagi and P. Fischer, *Nat. Rev. Mater.*, 2018, **3**, 113–124.
16 V. Garcia-Gradilla, J. Orozco, S. Sattayasamitsathit, F. Soto, F. Kuralay, A. Pourazary, A. Katzenberg, W. Gao, Y. Shen and J. Wang, *ACS Nano*, 2013, **7**, 9232–9240.
17 S. Debata, N. A. Kherani, S. K. Panda and D. P. Singh, *J. Mater. Chem. B*, 2022, **10**, 8235–8243.
18 K. Selvig and J. A. Alspaugh, *Mycobiology*, 2011, **39**, 249–256.
19 P. A. Lund, D. De Biase, O. Liran, O. Scheler, N. P. Mira, Z. Cetecioglu, E. N. Fernández, S. Bover-Cid, R. Hall, M. Sauer and C. O'Byrne, *Front. Microbiol.*, 2020, **11**, 556140.
20 N. M. Martinez-Rossi, G. F. Persinoti, N. T. A. Peres and A. Rossi, *Mycoses*, 2012, **55**, 381–387.
21 D. P. Singh, U. Choudhury, P. Fischer and A. G. Mark, *Adv. Funct. Mater.*, 2017, **29**, 1701328.
22 N. Möller, S. Seiffert, T. Palberg and R. Niu, *ChemNanoMat*, 2021, **7**, 1145–1160.
23 N. Möller, B. Liebchen and T. Palberg, *Eur. Phys. J. E*, 2021, **44**, 41.
24 J. Zhuang, R. W. Carlsen and M. Sitti, *Sci. Rep.*, 2015, **5**, 11403.
25 S. Heckel and J. Simmchen, *Advanced Intelligent Systems*, 2019, vol. 1, p. 1900093.
26 B. Ai and Y. Zhao, *Nanophotonics*, 2018, **8**, 1–26.
27 M. T. Taschuk, M. M. Hawkeye and M. J. Brett, *Handbook of Deposition Technologies for Films and Coatings*, Elsevier, 2010, pp. 621–678.
28 Y.-P. Zhao, D.-X. Ye, G.-C. Wang and T.-M. Lu, *Nano Lett.*, 2002, **2**, 351–354.
29 Y. He and Y. Zhao, *Nanoscale*, 2011, **3**, 2361.
30 J. G. Gibbs and P. Fischer, *Chem. Commun.*, 2015, **51**, 4192–4195.
31 P. Fischer and A. Ghosh, *Nanoscale*, 2011, **3**, 557–563.
32 D. P. Singh and J. P. Singh, *Appl. Phys. A*, 2014, **114**, 1189–1193.
33 D. P. Singh, S. Kumar and J. P. Singh, *RSC Adv.*, 2015, **5**, 31341–31346.
34 C. M. Maier, M. A. Huergo, S. Milosevic, C. Pernpeintner, M. Li, D. P. Singh, D. Walker, P. Fischer, J. Feldmann and T. Lohmüller, *Nano Lett.*, 2018, **18**, 7935–7941.
35 J. G. Gibbs and Y.-P. Zhao, *Small*, 2009, **5**, 2304–2308.
36 P. Basnet and Y. Zhao, *J. Mater. Chem. A*, 2014, **2**, 911–914.
37 S. Ghosh and A. Ghosh, *Nat. Commun.*, 2019, **10**, 4191.
38 G. Dunderdale, S. Ebbens, P. Fairclough and J. Howse, *Langmuir*, 2012, **28**, 10997–11006.
39 R. Golestanian, T. B. Liverpool and A. Ajdari, *New J. Phys.*, 2007, **9**, 126–126.
40 W. E. Uspal, M. N. Popescu, S. Dietrich and M. Tasinkevych, *Soft Matter*, 2015, **11**, 434–438.
41 J. L. Moran and J. D. Posner, *Annu. Rev. Fluid Mech.*, 2017, **49**, 511–540.
42 A. Rashidi, S. Razavi and C. L. Wirth, *Phys. Rev. E*, 2020, **101**, 042606.
43 R. Dong, Q. Zhang, W. Gao, A. Pei and B. Ren, *ACS Nano*, 2016, **10**, 839–844.
44 J. R. Howse, R. A. L. Jones, A. J. Ryan, T. Gough, R. Vafabakhsh and R. Golestanian, *Phys. Rev. Lett.*, 2007, **99**, 048102.
45 J. J. Anderson and L. John, *Annu. Rev. Fluid Mech.*, 1989, **21**, 61–99.
46 D. Saintillan, *Annu. Rev. Fluid Mech.*, 2018, **50**, 563–592.
47 S. E. Spagnolie and E. Lauga, *J. Fluid Mech.*, 2012, **700**, 105–147.
48 D. Nicholls, A. DeVerse, R. Esplin, J. Castañeda, Y. Loyd, R. Nair, R. Voinescu, C. Zhou, W. Wang and J. G. Gibbs, *ACS Appl. Mater. Interfaces*, 2018, **10**, 18050–18056.